

Photoinduced Structural Conversions of Transition Metal Chalcogenide Materials

M. Y. C. Teo,[†] S. A. Kulinich,^{†,‡} O. A. Plaksin,^{*,§,||} and A. L. Zhu^{*,†}

Department of Chemistry, University of British Columbia, 2036 Main Mall, Vancouver, BC, Canada V6T 1Z1, Department of Applied Sciences, University of Quebec, Saguenay, PQ, Canada G7H 2B1, Leypunsky Institute for Physics and Power Engineering, Obninsk, Kaluga Region, Russia 249033, and Obninsk State Technical University for Nuclear Power Engineering, Obninsk, Kaluga Region, Russia 249040

Received: December 22, 2009; Revised Manuscript Received: February 10, 2010

The conversions of NiAs-type structures of transition metal chalcogenides (FeS and CoSe) to pyrite-type structures of dichalcogenides (FeS₂ and CoSe₂, respectively) under irradiation by HeNe laser (wavelength, 632.8 nm; intensity, 6×10^4 W/cm²) have been investigated using Raman spectroscopy. The laser-induced conversions give rise to Raman peaks corresponding to vibrations of S–S or Se–Se bonds of respective pyrite structures. The results are of interest for the characterization and fabrication of pyrite-like structures necessary for applications as oxygen reduction reaction catalysts. Material modifications at the micrometer and submicrometer levels are attainable. The structural conversions are accompanied by self-polymerization of excess chalcogen. Extended laser irradiation (>500 s) in air induces the substitution of chalcogen (S or Se) by oxygen in the chalcogenide materials and the subsequent formation of transition metal (Fe or Co) oxides. Excess chalcogen appears to prevent further oxidation. The article also presents conditions necessary to avoid laser-induced structural changes and oxidation of metal chalcogenide materials during Raman measurements.

1. Introduction

Concerns of global warming from greenhouse gas emissions have increased interest in cleaner and more efficient energy sources such as fuel cells. Since the Kyoto protocol was signed, vast resources have been devoted to developing proton exchange membrane fuel cell (PEMFC) that uses hydrogen fuel and oxygen from air to produce electricity. Recently, various PEMFC demonstrations for power generation, transportation, and portable power have shown that the present technologies can perform reasonably well. However, one of the major obstacles for mass commercialization of PEMFC systems is their high cost due to the use of precious metal catalysts such as Pt.¹ The development of less expensive catalysts is therefore needed, especially for oxygen reduction reaction (ORR). According to the results of catalyst screenings conducted by different groups worldwide, one of the promising directions is the development of ORR catalysts based on transition metal–chalcogen combinations.² Recently, catalysts formed from transition metal chalcogenides with pyrite-type structure have been investigated as lower-cost alternatives to Pt for oxygen reduction at the cathode.^{3–7} Transition metal dichalcogenides were reported to have superior ORR catalytic performance over their monochalcogenide counterparts.⁷ The further investigations revealed that having the second chemical bond between transition metal and chalcogen atoms in pyrite structure provides up to twice the ORR catalytic activity than only having one chemical bond.⁷ In a chalcogen-rich environment, the NiAs-type structure of transition metal monochalcogenide can be converted to pyrite-

type structure, and this has reportedly increased the ORR catalytic activity of the material.⁷

The traditional approach to explore new potential catalysts has been to determine the activity of a dispersed catalyst onto a supporting substrate such as large-area carbon. However, such comparisons generally suffer from incomplete information because of different active surface areas, unknown surface composition and structure, as well as the detachment of catalyst powders during stability tests. For Pt research, CO stripping voltammetry in conjunction with the Bruner–Emmett–Teller (BET) method provides a well-established approach for determining the active area of Pt catalysts,^{8,9} but this approach is not applicable for many other catalysts. In particular, metal chalcogenide materials do not show any significant CO adsorption effect when compared with Pt. Therefore, the unknown active surface area limits direct electrochemical comparisons with the standard catalysts such as Pt-based catalysts. Initial work to prepare model Fe–S and Co–Se thin film catalysts was carried out to compare their catalytic activity with that of Pt directly as well as to establish a suitable analytical methodology to characterize the catalysts.^{3–5} Besides FeS₂, CoS₂, and CoSe₂-like thin films with pyrite structure that appeared especially active for ORR,^{4,5} it was also found that micro-Raman spectroscopy can play a unique role in characterizing both the surface and bulk (up to 1 μ m in depth) of transition metal chalcogenide materials for their crystal structures, chalcogen allotropes, as well as detecting oxide formation before and after electrochemical ORR evaluations.^{3–5}

This article is devoted to another finding, namely, the conversion reactions of FeS to FeS₂ and CoSe to CoSe₂ induced by a HeNe laser (632.8 nm) during Raman characterization. It is crucial to understand the mechanisms of such conversions not only because these conversion reactions are helpful to increase the ORR catalytic activity at transition metal chalcogen surfaces but also for proper Raman spectroscopic analysis of

* Corresponding authors. E-mail: plax@mail.ru (O.A.P.); researchman12001@yahoo.com (A.L.Z.).

[†] University of British Columbia.

[‡] University of Quebec.

[§] Leypunsky Institute for Physics and Power Engineering.

^{||} Obninsk State Technical University for Nuclear Power Engineering.

relevant samples. Consequently, this study demonstrates HeNe laser operating conditions necessary to (i) preserve the original state of transition metal chalcogenide, (ii) facilitate the transformation from FeS and CoSe in chalcogen rich materials to transition metal dichalcogenides such as FeS₂ and CoSe₂, respectively, and (iii) induce the conversion to transition metal oxides.

2. Experimental Section

2.1. Preparation of Fe–S and Co–Se Thin Films. A dual magnetron sputter coating system (model V3T, Corona Vacuum Coaters, Inc.) with two cylindrical targets (5 cm diameter, 0.6 cm thick) was used for fabrication of Fe–S and Co–Se thin films that are well-adhered onto glassy carbon (GC) substrates. GC substrates (Tokai Carbon) were polished and cleaned with the procedure reported elsewhere.³ Inside the coating system, the GC substrates (target bias -75 V) were oriented to face respective sputtering targets. An operating pressure of 3.5×10^{-3} torr was maintained during sputter deposition.

The first film was fabricated by sputtering a FeS target prepared in-house by subjecting FeS powder (99.9%, Sigma Aldrich) to a pressure of 50 psi. To increase the adhesion, a thin Ta sublayer was deposited onto the GC substrate by applying DC power (50 W) to a commercial Ta target (99.9%, Angstrom Sciences) that was mounted next to the FeS target inside the sputter system. Deposition of a Fe–S thin film on top of the Ta layer was achieved by applying RF power (38 W) to the FeS target alone. The resulting well-adhered thin film (denoted TF1) had a S/Fe ratio of 1.0 according to energy dispersive X-ray spectroscopy (EDX) analysis, which suggested that a stoichiometric FeS film had been fabricated. The other Fe–S film discussed here (denoted TF2) was prepared by applying RF power (38 W) to a commercial FeS₂ target (99.9% purity, Angstrom Sciences) and DC power (50 W) to a Fe-rich mild-steel target such that EDX showed a S/Fe ratio of 2.0, which is consistent with stoichiometric FeS₂. Prior to film fabrication, all targets were Ar ion sputtered for cleaning purposes. As for the preparation of the Co–Se thin film, commercial Co and Se targets were used. A detailed description can be found elsewhere.^{3,6} The thicknesses of all prepared films were ~ 400 nm.

2.2. Preparation of Carbon Powder Supported CoSe₂. CoSe₂ supported on carbon powder was synthesized for use as a catalyst in the study. Carbon powder (1 g, XC72R powder, Cabot) was dispersed into a beaker filled with 1 L of ultrapure deionized water (NCCLS type 1, 18.2 M Ω cm); 50 mL of isopropanol (Fisher Scientific) was introduced to aid wetting, and this was followed by the addition of 10.2 g of CoSO₄·7H₂O (99%, Sigma) and 8.2 g of SeO₂ (99.9%, Aldrich). After 1 h of magnetic stirring, 3.2 g of NaBH₄ (99% purity, Sigma-Aldrich) was added to the solution. The complete addition of NaBH₄ was followed by another 1 h of stirring. The nascent powder was filtered, washed twice with deionized water (type 1), and dried in air. The dried powder was then placed into a porcelain combustion boat and introduced to a tube furnace (model 79300, Thermolyne), where it was heated to 600 °C for 4 h under an Ar atmosphere. The resulting supported CoSe₂ on carbon powder was ground (by mortar and pestle) prior to its XRD characterization.

2.3. Characterization Methods. The thin films were characterized with regard to their bulk composition by EDX measurements taken with a Hitachi S2300 spectrometer (20 keV incident electron beam), whereas X-ray photoelectron spectroscopy (XPS) was used for an overall characterization of the

surface composition. The latter used a Leybold MAX200 spectrometer with the Mg K α (1253.6 eV) source operated at 10 kV, 20 mA, with pressure in the analytical chamber at 1.5×10^{-9} torr. Survey and higher-resolution XPS spectra were measured with pass energies of 192 and 48 eV, respectively, and the binding energies (BEs) were referenced to the C 1s peak for adventitious hydrocarbon contamination at 285.0 eV. Auger electron spectra and scanning electron micrographs were obtained using a scanning Auger microprobe (SAM) system (Microlab 350, Thermo Electron Corp), which was equipped with a hemispherical energy analyzer and field emission source (10 keV, 3.5 nA).

Limited by the inelastic mean free path of electron, XPS has a probing depth of ~ 8 nm with a detection limit of ~ 0.1 at. %. SAM also provides surface composition information, similar to that of XPS, but utilizes an electron beam capable of providing spatial resolution of down to 10 nm for analyzing micro- and nanostructures. EDX uses an electron beam to interact with the analyzed sample to generate characteristic X-rays emitted from a depth of several micrometers. Therefore, XPS and SAM give elemental and chemical information on sample surfaces, whereas EDX, in comparison, provides bulk composition of thin films. For assessing potential ORR catalysts, characterizing their surfaces is essential because the catalysis reactions occur at the surface, and the as-prepared thin films may have different surface and bulk compositions.

Micro-Raman spectroscopy was also used for characterizing transition metal chalcogenide materials, particularly for studying laser-induced conversions. Raman spectra were acquired using the 632.8 nm line of a helium–neon (HeNe) laser (Renishaw inVia Raman Microscope) and a 20 \times objective (numerical aperture of 0.40). Each Raman spectrum was acquired with the output laser power, P , not higher than 0.5 mW by coadding the different scans for the particular total exposure time. Maximum laser intensity, $I = 4P/\pi d^2$, estimated by taking into account the diameter, d , of the laser spot on the sample surface (~ 1 μ m), was approximately equal to 6×10^4 W/cm². Before each measurement, the instrument was calibrated with a standard Si sample (520 cm⁻¹), and all spectra were reproducible to ± 2 cm⁻¹.

Crystalline structures of synthetic powder samples and high purity FeS₂ mineral pyrite (Zacatecas, Mexico) that had been ground to a fine powder by mortar and pestle were examined with X-ray diffraction (XRD). Measurements were made with a Bruker D8 advanced diffractometer (Bruker, Germany) using a Cu K α radiation source (wavelength 1.5418 Å) with the scattering angle (2θ) varying from 5 to 90° at 0.02° s⁻¹ of scan speed. Standard XRD patterns of FeS₂ and CoSe₂ can be found in literature.^{7,10,11} Both crystalline FeS₂ (Zacatecas, Mexico) and CoSe₂ powders were of high purity (also confirmed by the Laboratory of Mineral Identification of the University of British Columbia) and were thus used as the internal reference standards for XPS and Raman experiments.

Structure of the CoSe thin film was studied with high-resolution transmission electron microscopy (HRTEM). The sample slices were made using an ultramicrotome (MT6000 Sorvall) with diamond knife and collected from a bath of double-distilled water onto 400 mesh TEM copper grids and then dried at room temperature. Cross-sectional samples were analyzed with a Tecnai G² instrument (FEI) equipped with a field emission source (F20 model) operating at 200 kV for local imaging, diffraction, and EDX. Prior to measurements, the instrument was calibrated with an Au standard sample provided by the manufacturer.

3. Results and Discussion

3.1. Fe–S Crystal Structure and Raman Modes. Two crystal structures, troilite and pyrrhotite, are known for FeS. Both forms are of a prototypical NiAs crystal structure.¹² In troilite, each Fe atom is octahedrally coordinated to six S atoms, whereas in pyrrhotite, S is both five- and six-fold coordinated because of metal vacancies. Pyrrhotite is also known for having two structural types, namely, hexagonal D_{6h}^4 and monoclinic C_{2h}^4 . The surface crystal structure of troilite or pyrrhotite forms of FeS can be identified using XPS.¹³ In this study, the crystalline structure of TF1 sample was identified as pyrrhotite. Pyrrhotite exhibits neither first-order nor second-order Raman spectrum because of its structural symmetry, and no infrared absorption band was observed because of its metallic properties.¹⁴

The crystal structure of FeS₂ pyrite is cubic (space group T_h) with four formula units per unit cell.¹⁵ The Fe atoms occupy the sites of a face-centered cubic sublattice, and the S atoms are arranged in dumbbell pairs along (111) directions located at the midpoints of the cube's edges and body center. In a distorted octahedron, the six nearest-neighbor S atoms coordinate each Fe atom, and each S atom is bonded to three Fe and one other S atom, forming a distorted tetrahedron. The FeS₆ octahedrons are linked by corner sharing. The irreducible representation of the vibrations of FeS₂ pyrite is $G = A_g + E_g + 3T_g + 2A_u + 2E_u + 6T_u$. Raman active modes comprise of a symmetric mode (A_g), one doubly degenerate mode (E_g), and three triply degenerate modes (T_g). Raman-active modes only involve the movements of the S atoms and not of the Fe atoms. The A_g mode and one of T_g modes correspond to in-phase and out-of-phase stretching vibrations of the S₂ dumbbells, respectively. In the E_g vibrational mode, S atoms are displaced perpendicular to the S–S bond axis. Two T_g modes correspond to various combinations of librational and stretching motions.¹⁶

A large variety of Raman spectra have been reported for FeS₂^{16,17} and the references therein. Locations of Raman peaks depend on the surface state (isotropic, anisotropic, purity), crystal structure (pyrite or marcasite), temperature, and pressure. For example, narrow peaks at 343 (E_g), 350 (T_g), 377 (T_g), 379 (A_g), and 430 (T_g) cm^{-1} are resolved for FeS₂ pyrite single crystals in different scattering configurations.¹⁷ The first T_g peak is very weak, and the height of the second T_g peak (corresponding to out-of-phase stretching of S–S bonds) is about a half of that for the A_g peak. For polycrystalline materials, the A_g and E_g peaks cannot be resolved from the T_g peaks. High-purity, crystalline FeS₂ with a pyrite structure usually exhibits three characteristic Raman peaks at 341–353 (E_g , T_g), 377–383 (A_g , T_g), and 427–446 (T_g) cm^{-1} .^{14,17–19} In this article, the first band is called “ E_g peak” for brevity, and the second band is called “ A_g peak”, although these peaks could be contributed from T_g modes as well.

3.2. Fe–S Powders. Prior to the Raman experiment for the FeS powder sample, a Raman spectrum of high purity Zacatecas FeS₂ with pyrite structure⁵ was recorded as an internal standard. The tested surface was freshly cleaved in Ar flow prior to Raman measurements. Raman peak locations (341, 376, and 425 cm^{-1}), shapes, and relative intensities (Figure 1a) are consistent with previously reported data.^{14,17–19}

The laser photon energy ($\hbar\omega = hc/\lambda = 1.97$ eV) was higher than the band gap for both FeS₂ (0.92 eV) and FeS (0.5 eV). That is, the laser photon energy corresponded to interband electron transitions. The optical absorption coefficient α for interband transitions in FeS₂ (allowed direct transitions) is equal to 2×10^4 cm^{-1} at 1.97 eV.²⁰ Accordingly, the laser radiation

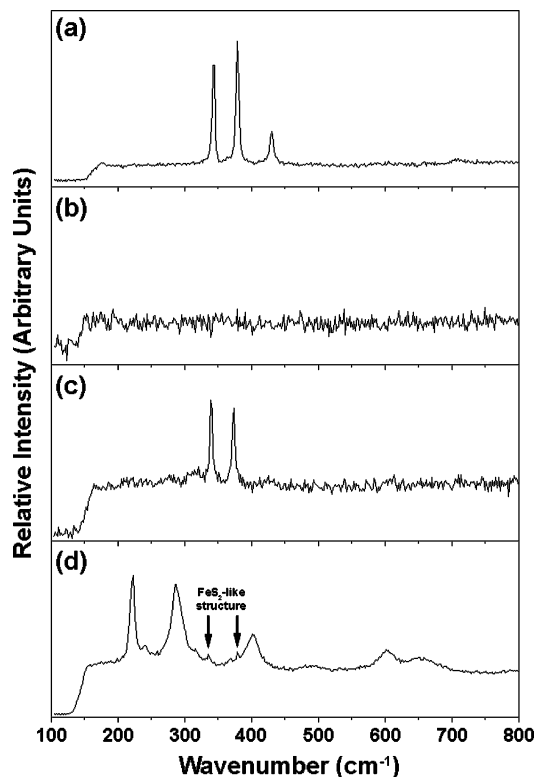


Figure 1. Raman spectra of (a) Zacatecas FeS₂ mineral pyrite as well as high-purity FeS powder for different laser exposure times of (b) 100, (c) 500, and (d) 1,000 s.

penetrated no deeper than ~ 500 nm (because penetration depth is about α^{-1}). It is worth noting that the laser-induced interband transitions result in accumulation of free electrons in the conduction band, and the collective motion of free electrons contributes to optical absorption. Concentration, n_e , of free electrons and, subsequently, the plasma frequency, ω_p , depends on both the laser intensity, I , and the time of electron–hole recombination, τ , in accordance with the formulas: $n_e = \alpha I \tau / \hbar\omega$ and $\omega_p = e\sqrt{n_e/\epsilon_0 m_e}$, where e is the elementary charge, ϵ_0 is the permittivity of free space, and m_e is the electron mass. (See examples in ref 21.) A significant contribution of free electrons to optical absorption takes place at $\hbar\omega_p > \hbar\omega$, and accordingly, at the electron lifetime and electron concentration exceeding approximately 10^{-14} s and 10^{13} cm^{-3} , respectively. It is noted that the time of 10^{-14} s is very close to the lower limit for electron–hole recombination time in solids. For many materials, this time is several orders of magnitude longer. Accordingly, the concentration of laser-induced free electrons and optical absorption are expected to be higher than 10^{13} cm^{-3} and 2×10^4 cm^{-1} , respectively. In contrast, an increase in optical reflection due to plasma oscillations decreases the laser energy absorbed. Although the optical absorption and reflection are competing phenomena, increase in the former decreases penetration depth of laser radiation. Therefore, the changes in Raman spectra reported in this and the following sections are an indication of reactions in submicrometer layers.

Raman measurements for the commercial FeS powder (99.9%, Sigma Aldrich) showed no Raman peaks for irradiation times shorter than 500 s, as seen in Figure 1b. Laser irradiation for a time period of 500 s typically gave rise to Raman peaks at 339 and 373 cm^{-1} (Figure 1c), which were close to the two strongest peaks of a FeS₂ pyrite structure (341 and 376 cm^{-1} , respectively). The T_g peak at 420–430 cm^{-1} did not appear. Furthermore, the intensity of the E_g peak at 339 cm^{-1} was larger

than that of the A_g peak at 373 cm^{-1} in contrast with relative peak intensities typically observed for FeS_2 (Figure 1a). This suggests that the laser irradiation did not result in complete conversion to pyrite phase but caused the formation of an intermediate structure. In particular, T_g modes should be observable for domains of FeS_2 not smaller than a unit cell comprising of four S–S pairs because of the complexity of the corresponding normal vibrations. In contrast, ordinary stretching and libration of S–S bond, responsible for A_g and E_g modes, may take place in a cluster even if it comprises a single dumbbell S_2 unit. Accordingly, the inverse relation of A_g and E_g peaks could be explained by the absence of contributions from the T_g modes. Because FeS is sulfur deficient compared with FeS_2 , the formation of both S–S pairs and sulfur-free space should occur simultaneously. In other words, laser irradiation initiated inhomogeneity of sulfur distribution, resulting in shifts of S atoms within unit cells of FeS. Beyond 1000 s of HeNe laser exposure, new Raman peaks at 222, 238, 285, 402, 602, and 650 cm^{-1} attributed to $\alpha\text{-Fe}_2\text{O}_3$ ^{22–24} were observed. Simultaneous growth of peaks at 222 and 238 cm^{-1} probably indicates the presence of polysulfides, namely, rearrangement of S-chain molecules to S-ring molecules during oxidation.²⁵ Figure 1d shows that Raman peaks at 339 and 373 cm^{-1} were still detectable, indicating that the FeS_2 -like structures are still present. These findings suggest that a longer HeNe-laser irradiation stimulates the formation of chemical bonds between oxygen and iron on the surface of crystalline FeS and causes S atoms to redistribute at the surface and the deeper regions (due to the diffusion of sulfur and/or to outflow of iron). Accordingly, FeS pyrrhotite experiences a short-order rearrangement of S atoms with the formation of separated S–S pairs, randomly oriented and/or with spatial separation longer than the distance between adjacent S–S pairs in a regular pyrite structure. Extended laser irradiation results in both the formation of detectable $\alpha\text{-Fe}_2\text{O}_3$ phase and the almost complete removal of S atoms from the surface layer (about 1 nm in thickness) to a deeper sublayer. This explanation is consistent with the results reported previously on air-oxidation of pyrrhotite.²⁶

3.3. Fe–S Thin Films. 3.3.1. Characterization of the As-Prepared Fe–S Thin Films. As-prepared thin films, TF1 and TF2 had overall bulk S/Fe ratios of 1.0 and 2.0, respectively, according to EDX measurements. XPS detected oxygen and carbon on the surfaces of the as-prepared films, but corresponding signals disappeared after 2 min of Ar ion bombardment, indicating that these additional elements arose from adventitious contamination due to exposure of the samples in air. High-resolution XPS spectra seen in Figures 2, 3, and 4 highlight the chemical state differences between TF1 and TF2. Figure 2 shows two peaks in the S 3s region with binding energies (BEs) at 13.5 and 16.6 eV, respectively, for TF2 and a single peak with BE at 13.4 eV for TF1. This is consistent with the monosulfide species being predominant on TF1, whereas both disulfide and monosulfide components are present on TF2.^{27,28} Figure 3 shows sharp Fe $2p_{1/2}$ and Fe $2p_{3/2}$ peaks at 720.6 and 707.7 eV, respectively, for TF2, which are attributed to FeS_2 .^{27,28} In contrast, TF1 showed broad Fe $2p_{1/2}$ and $2p_{3/2}$ peaks at 724.8 and 710.9 eV, respectively, and this is consistent with FeS.^{27,28} Figure 4a,b shows S 2p spectra of (a) TF1 and (b) TF2 in which each curve was fitted with three components. Accordingly, TF1 is predominantly attributed to S^{2-} (161.9 eV) with smaller amounts of S_2^{2-} and S^0 (163.0 and 164.3 eV, respectively), while TF2 is primarily attributed to the S_2^{2-} species (163.0 eV), with smaller amounts of S^{2-} and S^0 (161.9 and 164.3 eV, respectively) present.^{27–32} Overall, TF1 and TF2 were primarily FeS

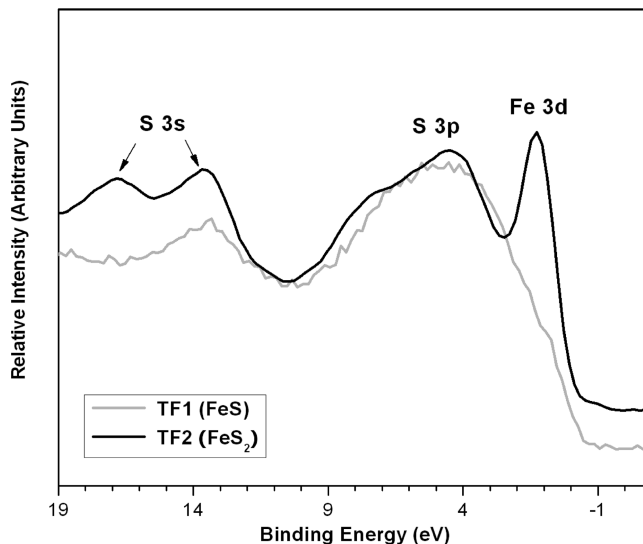


Figure 2. XPS valence region spectra for Fe–S thin films TF1 (gray line) and TF2 (black line).

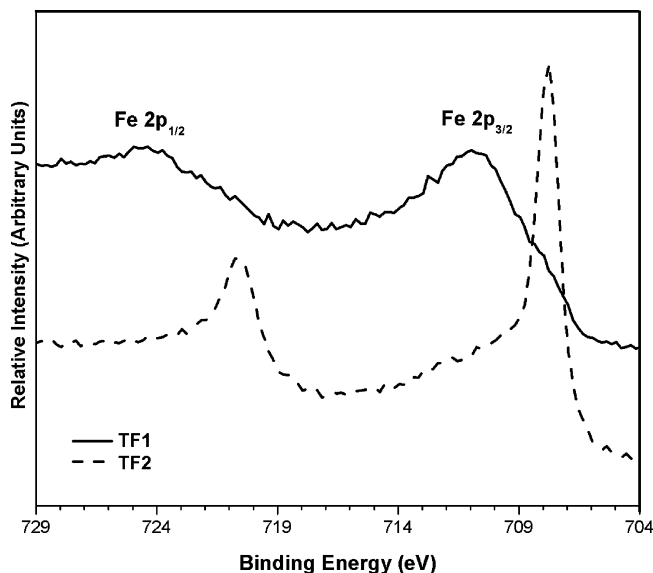


Figure 3. XPS Fe 2p spectra for Fe–S thin films TF1 (solid line) and TF2 (dashed line).

and FeS_2 films, respectively, although they could have some heterogeneity.

3.3.2. Raman Spectra Changes of Fe–S Thin Films. Figure 5 shows the Raman spectrum of as-prepared TF2 displaying three well-pronounced peaks at 340, 378, and 418 cm^{-1} and a broadband between 440 and 500 cm^{-1} . The former three peaks are in close agreement with our internal standard (341, 376, and 425 cm^{-1}) and with literature on anisotropic pyrite (342, 377, and 428 cm^{-1}).¹⁴ The broadband is associated with polysulfides (S_n^{2-} , where $2 \leq n \leq 8$) formed during the magnetron sputter deposition of the thin films. The E_g peak (340 cm^{-1}) for TF2 has a larger intensity compared with the A_g peak (378 cm^{-1}). Intensities of these peaks are in an inverse relation when compared with that typically observed for pyrite.¹⁹ The T_g peak emerges at a lower wavenumber (418 cm^{-1}) than that for a typical spectrum of pyrite (425 cm^{-1}) or the internal FeS_2 standard (428 cm^{-1}). It is worth noting that the position of the A_g peak (associated with in-phase S–S bond stretching) is almost the same for these materials. Consequently, the shift of the T_g peak to lower frequencies cannot be attributed to the softening of S–S bonds. However, it is evident that domains

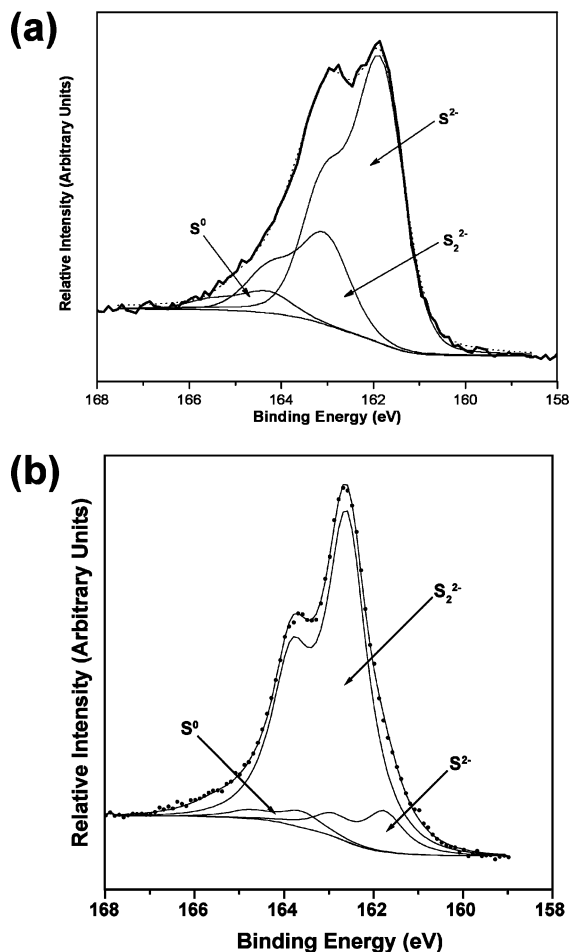


Figure 4. XPS S 2p spectra curve fitted for (a) TF1 and (b) TF2.

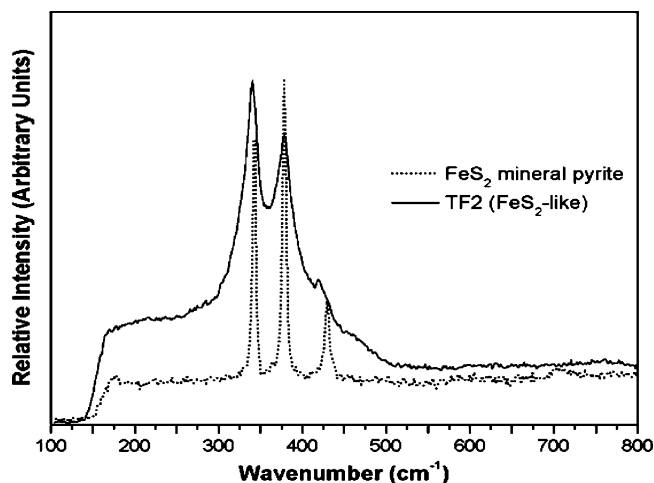


Figure 5. Raman spectra of Zacatecas FeS_2 mineral pyrite (gray dash line) and TF2, the FeS_2 -like thin film (solid black line).

of pyrite structure in the TF2 sample must be large enough to allow the T_g peak to appear. The domains must at least be larger than those in the laser-irradiated FeS powder, for which the peak was not observed. Estimations from XRD data, with the help of the Scherer formula, showed that the domain size for the TF2 was ~ 30 nm. If the domains are distorted compared with the regular pyrite structure, some misalignment of adjacent S—S pairs may take place, giving rise to the shift of the T_g peak.

No detectable changes were observed on the TF2 sample surface after irradiation by the HeNe laser after shining the

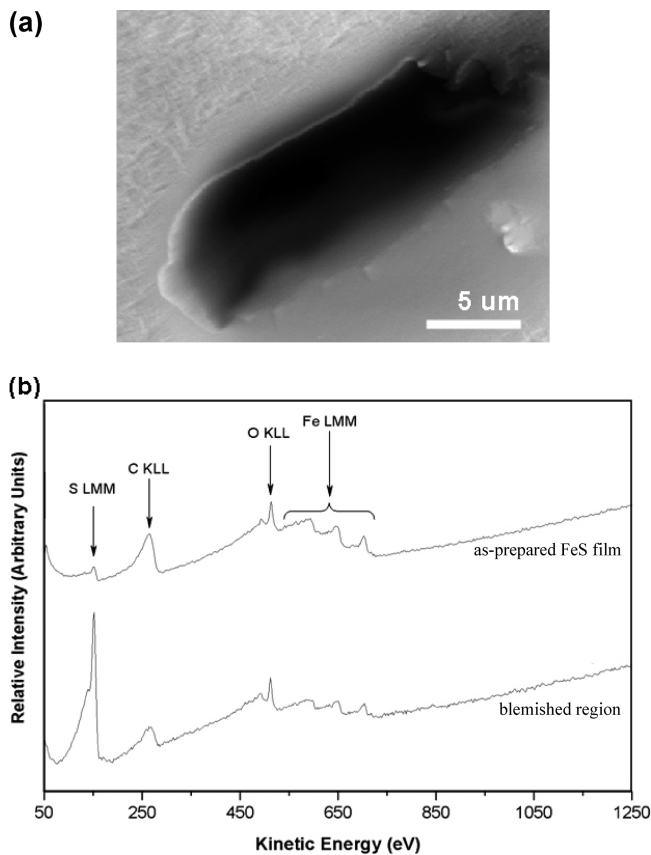


Figure 6. (a) SEM micrograph of blemish on FeS thin film (TF1) after HeNe laser exposure for 500 s. (b) Auger spectra from as-prepared TF1 and blemish region on TF1 after HeNe laser exposure for 500 s.

surface for >1000 s, which is in contrast with the results observed for the FeS thin film, TF1. Laser irradiation of the TF1 sample reveals the effect of local excesses of sulfur on the laser-induced conversion. Irradiation for <500 s resulted in no Raman peaks. This result is similar to that observed for the FeS powder. However, Figure 6a shows that irradiation for 1000 s resulted in a distinct localized (micrometer-sized) blemish on the originally smooth surface of TF1. Figure 6b represents the Auger electron spectra from the original surface and the localized blemish. Irradiation is seen to give rise to a marked increase in the S/Fe atomic ratio from 2.0 to 16.0.

Figure 7 displays the Raman spectrum from the laser-modified region of TF1 with broad peaks at around 339, 375, and 454 cm^{-1} . The first and second peaks suggest that a FeS_2 pyrite-like structure was formed. The T_g modes are not allowed for this structure, as it was also found for irradiated FeS powder. The intensity of the E_g peak (339 cm^{-1}) is larger than that of the A_g peak (375 cm^{-1}), as was observed for the TF2 and irradiated FeS powder. Broader Raman peaks of irradiated TF1 compared with other materials indicate more disorder in the FeS_2 pyrite-like structure.³⁵ Raman spectra in Figures 1 and 7 show that the formation of S—S pairs is a dominant factor in the structure transformations observed for both FeS powder and TF1 sample. This viewpoint is supported by the study of FeS and FeS_2 structures via near edge X-ray absorption fine structure technique.³⁶

Figure 7 also shows that the small peak at 454 cm^{-1} in the Raman spectrum of the irradiated TF1 is associated with polysulfides (FeS_n) in the blemished area.³³ The latter peak was not observed in Raman spectra of the FeS powder. The formation of FeS_n with random n probably contributes to the

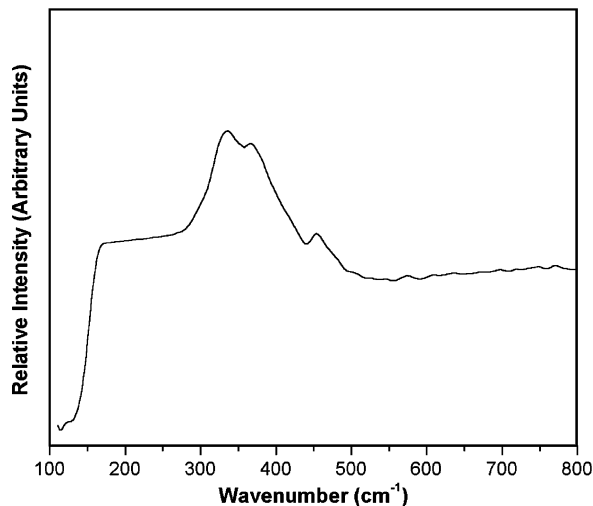


Figure 7. Raman spectrum of blemish region on TF1 (FeS thin film) after HeNe laser exposure for 1000 s.

broadening of the E_g and A_g peaks, as seen in Figure 7. This suggests that the laser irradiation has increased the local concentration of sulfur and facilitated formation of local FeS_2 bonding configurations (a pyrite-like structure) through a reaction proposed in the papers,^{37,38} that is, $\text{FeS} + \text{S} + h\nu \rightarrow \text{FeS}_2$.

The changes in irradiated regions of the TF1 film are consistent with thermodynamics. At room temperature, FeS in the presence of excess sulfur can be converted to FeS_2 : $\Delta G_f^\circ = -58 \text{ kJ mol}^{-1}$.³⁹ Laser irradiation with intensity I of $6 \times 10^4 \text{ W/cm}^2$ gave rise to an increase in the local temperature. According to the formula $\Delta T = I/\alpha\lambda$, where α and λ are the optical absorption coefficient (2×10^4 to 10^7 cm^{-1}) and thermal conductivity (about 40 W/mK), respectively, the temperature variation ΔT was in the range from 8 to 150 K. The upper limit of ΔT was estimated by taking into account the optical absorption (up to 10^7 cm^{-1}) by laser-induced free electrons. The penetration depth of laser irradiation corresponding to the upper limit of ΔT is $\sim 10 \text{ nm}$, which is typical for metals.²¹ At 450 K, ΔG calculated using data provided in ref 39 is equal to -190 kJ mol^{-1} . If there were no excess amounts of sulfur in the film, then extended laser irradiation in air would result in further conversion from FeS_2 -like structures to Fe_2O_3 . The corresponding ΔG_f° value is equal to -742 kJ mol^{-1} .⁴⁰ The S-rich environment is likely to prevent further oxidation.

3.4. Co–Se Systems. Two types of samples, (1) magnetron-sputtered CoSe thin film with excess Se (84 at. % Se, 16 at. % Co) and (2) high purity (according to XRD and SAM analyses) CoSe_2 supported on carbon powder, were irradiated by the HeNe laser. Figure 8a shows that CoSe_2 supported on carbon powder has a distinct Raman peak at 187 to 188 cm^{-1} ; this is the same position as previously reported for the A_g Raman mode of pyrite-type CoSe_2 single crystals.¹⁹ By increasing irradiation time from 100 to 500 s, Figure 8b shows an additional peak at 167–175 cm^{-1} . This peak can be attributed to a CoSeO complex,⁶ that is, a possible structural unit of CoSe_2O_5 and/or CoSeO_3 .⁴¹ Beyond 1000 s of exposure, Figure 8c shows the Raman spectrum being composed of peaks attributed to Co oxide (strongest at 484 and 691 cm^{-1}), CoSe_2 (187–188 cm^{-1}), and the CoSeO complex (167–175 cm^{-1}). This indicates that the laser-induced transformations in CoSe_2 occur in a similar manner as in FeS_2 , with a partial progressive substitution of Se by O.

The HRTEM micrograph in Figure 9 shows that the structure of as-prepared CoSe thin film comprises CoSe nanocrystals

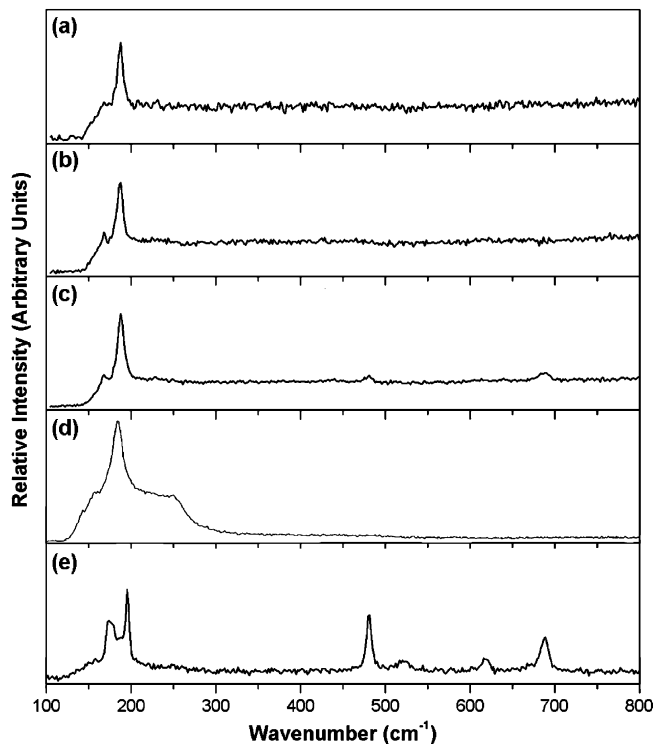


Figure 8. Raman spectra from Co–Se samples after different exposures to He–Ne laser: (a) CoSe_2 on carbon powder, 100 s exposure (laser power $<0.5 \text{ mW}$ on sample surface); (b) CoSe_2 on carbon powder, 500 s ($<0.5 \text{ mW}$); (c) CoSe_2 on carbon powder, 1000 s exposure ($<0.5 \text{ mW}$); (d) Co–Se thin film (84 at.% of Se, 16 at.% of Co) after 500 s exposure ($<0.5 \text{ mW}$); and (e) center hole region of a Co–Se thin film (84 at.% of Se, 16 at.% of Co) after 50 s exposure ($<5 \text{ mW}$).

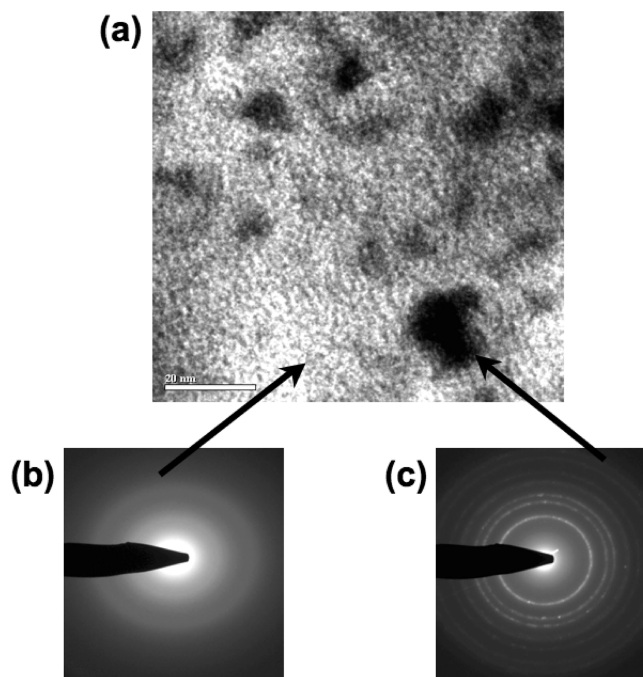


Figure 9. (a) High-resolution TEM micrograph of CoSe thin film (84 at.% of Se and 16 at.% of Co) structure with selected area electron diffraction of (b) bright regions (Se-rich regions) and (c) dark regions (highly crystalline Co–Se nanoparticles). Scale bar in (a) indicates 20 nm.

embedded into an amorphous Se matrix. The structure of the CoSe nanocrystals is of NiAs type.^{3,12} The CoSe thin film was irradiated at two fixed laser powers (about 0.5 mW and 5 mW). Laser irradiation of the CoSe film at the lower power (0.5 mW,

500s) gave rise to a peak at 181–184 cm^{-1} and a broadband at 130–280 cm^{-1} in the Raman spectrum (Figure 8d). The former Raman peak (slightly shifted when compared with CoSe_2 single crystals) was attributed to in-phase stretching vibrations of Se–Se pairs in a CoSe_2 -like structure. The laser irradiation caused the nanocrystals (dark dots in HRTEM image, Figure 9) to increase in size, whereas the corresponding diffraction pattern became more distinctive and complex: the number of rings and their intensity increased. Previous studies have shown that Raman peaks at 251–253 cm^{-1} can be attributed to Se_8 rings, whereas peaks at 141, 233 to 234 cm^{-1} can be due to Se_n chains.^{42–49} Polyselenides (Se_n^{2-}) can give rise to the peak at 269 cm^{-1} .⁵⁰ The observed broadband at 130–280 cm^{-1} covers the characteristic locations of Raman peaks corresponding to the various types of Se listed above. Peak broadening also suggests the presence of amorphous Se.⁵¹

Extended laser irradiation of the CoSe film at the lower power did not result in any significant Raman spectrum change, suggesting that excess Se prevented further oxidation. However, laser irradiation at the higher power (5 mW, intensity $\sim 6 \times 10^5 \text{ W/cm}^2$) resulted in a localized blemish whose topography was similar to that shown in Figure 6a. Figure 8e shows that additional Raman peaks associated with Co oxide (198, 484, 523, 622, 693 cm^{-1})^{42,43} and a CoSeO complex (167–175 cm^{-1})^{42–44} do emerge in the Raman spectrum taken over the blemish area.

The results of laser irradiation of the CoSe thin film are also consistent with thermodynamics. In an Se-rich environment, CoSe_2 is favored over nonstoichiometric CoSe (values of ΔG_f° –122 and –73 kJ mol^{-1} , respectively³⁹), although Co oxides eventually become favored in the presence of oxygen (values of ΔG_f° range from –214 to –744 kJ mol^{-1} , depending on the particular oxide⁴⁰).

4. Concluding Remarks

Transition metal dichalcogenides were recently demonstrated to have ORR catalytic activity comparable to Pt-based catalysts prevalently used in current fuel cells. They also showed superior ORR catalytic activity when compared with their monochalcogenide counterparts. This study demonstrates that HeNe laser irradiation induces conversions of NiAs-type structures of transition metal chalcogenides (FeS and CoSe) to pyrite-type structures of dichalcogenides (FeS_2 and CoSe_2 , respectively). The laser-induced conversions can be detected via Raman spectroscopy. Laser irradiation initiates the formation of chalcogen pairs (S–S or Se–Se) and gives rise to Raman peaks corresponding to vibrations of S–S or Se–Se bonds in pyrite-like structures. The structural conversions are accompanied by self-polymerization of excess chalcogen. Extended laser irradiation (>500 s) induces the substitution of chalcogen (S or Se) by oxygen in the chalcogenide materials and the subsequent formation of transition metal (Fe or Co) oxides. Excess chalcogen inhibits oxidation in the transition metal chalcogenide materials. The observed conversions are summarized in Scheme 1. This study also points to the importance of appropriate conditions for manipulating Raman measurements. Recommendations include (a) laser operation at low intensity ($< 6 \times 10^4 \text{ W/cm}^2$) and (b) short acquisition times ($< 500 \text{ s}$) to avoid laser-induced structural changes and oxidation.

The observed laser-induced conversions are interesting in light of the potential use in synthesis of ORR catalysts. Because laser-induced modification at the micrometer lateral resolution and submicrometer depth resolution is attainable, laser irradiation can be used deliberately for the fabrication of transition metal

SCHEME 1

FeS powder:

$\text{FeS} + \text{hv}$

→ FeS_2 pyrite-like structure + hv

→ Fe oxide + FeS_2 pyrite-like structure

FeS thin film (with excess S):

$\text{FeS} + \text{S} + \text{hv}$

→ FeS_2 pyrite-like structure + poly-sulfides (S_n^{2-})

CoSe₂ supported on carbon powder:

$\text{CoSe}_2 + \text{hv}$

→ CoSe_2 + CoSeO complex + hv

→ Co oxide + CoSeO complex + CoSe_2

Co-Se thin film (84 at.% Se, i.e. excess Se):

$\text{CoSe} + \text{Se} + \text{hv}$

→ CoSe_2 -like structure + Se + hv

→ Co oxide + CoSeO complex + CoSe_2 -like structure

dichalcogenide materials with pyrite-like structures necessary for applications as ORR catalysts. Studies on FeS formation and oxidation processes are also a topic of interest in oceanology and geochemistry.⁵² Together with the methodology described in this article, the results presented here may help deepen understanding in geobiochemistry and ocean chemistry research.

Acknowledgment. We acknowledge the research support by the Natural Sciences and Engineering Research Council of Canada and the financial support by the Russian National Foundation for Basic Research (grants 09-02-97526 and 09-03-01039). We also thank the Lab of Mineral Identification, Department of Geography, University of British Columbia for providing the high purity FeS samples.

References and Notes

- (1) Srinivasan, S.; Mosdale, R.; Stevens, P.; Yang, C. *Annu. Rev. Energy Environ.* **1999**, *24*, 281–328.
- (2) *PEM Fuel Cell Electrocatalysts and Catalyst Layers: Fundamentals and Applications*; Zhang, J. J., Ed.; Springer: London, 2008.
- (3) Susac, D.; Sode, A.; Zhu, L.; Wong, P. C.; Teo, M.; Bizzotto, D.; Mitchell, K. A. R.; Parsons, R. R.; Campbell, S. A. *J. Phys. Chem. B* **2006**, *110*, 10762–10770.
- (4) Zhu, L.; Susac, D.; Teo, M.; Wong, K. C.; Wong, P. C.; Parsons, R. R.; Bizzotto, D.; Mitchell, K. A. R.; Campbell, S. A. *J. Catal.* **2008**, *258*, 235–242.
- (5) Susac, D.; Zhu, L.; Teo, M.; Wong, P. C.; Wong, K. C.; Bizzotto, D.; Mitchell, K. A. R.; Parsons, R. R.; Campbell, S. A. *J. Phys. Chem. C* **2007**, *111*, 18715–18723.
- (6) Teo, M.; Wong, P. C.; Zhu, L.; Susac, D.; Campbell, S. A.; Mitchell, K. A. R.; Parsons, R. R.; Bizzotto, D. *Appl. Surf. Sci.* **2006**, *253*, 1130–1134.
- (7) Zhu, A. L.; Teo, M.; Wong, P. C.; Wong, K. C.; Narita, I.; Ernst, F.; Mitchell, K. A. R.; Campbell, S. A. Synthesis and characterization of supported CoSe_2 as a catalyst for the oxygen reduction reaction. *Appl. Catal., A*, submitted.
- (8) Jusys, Z.; Kaiser, J.; Behm, R. *Phys. Chem. Chem. Phys.* **2001**, *3*, 4650–4660.
- (9) Maillard, F.; Savinova, E. R.; Simonov, P. A.; Zaikovskii, V. I.; Stimming, U. *J. Phys. Chem. B* **2004**, *108*, 17893–17904.
- (10) Tanaka, K. *Solid State Commun.* **1980**, *34*, 201–204.
- (11) International Center for Diffraction Database, PDF 03-065-3327 (CoSe_2).
- (12) Crystal Lattice Structures. <http://cst-www.nrl.navy.mil/lattice> (accessed Feb 2008).
- (13) Skinner, W. M.; Nesbitt, H. W.; Pratt, A. R. *Geochim. Cosmochim. Acta* **2004**, *68*, 2259–2263.

- (14) Mernagh, T. P.; Trudu, A. G. *Chem. Geol.* **1993**, *103*, 113–127.
- (15) Stevens, E. D.; DeLucia, M. L.; Coppens, P. *Inorg. Chem.* **1980**, *19*, 813–820.
- (16) Sourisseau, C.; Cavagnat, R.; Fouassier, M. *J. Phys. Chem. Solids* **1991**, *52*, 537–544.
- (17) Vogt, H.; Chattopadhyay, T.; Stolz, H. J. *J. Phys. Chem. Solids* **1983**, *44*, 869–873.
- (18) Kelppe, A. K.; Jephcoat, A. P. *Mineral. Mag.* **2004**, *68*, 433–441.
- (19) Anastassakis, E.; Perry, C. H. *J. Chem. Phys.* **1976**, *64*, 3604–3609.
- (20) Abass, A. K.; Ahmed, Z. A.; Tahir, R. E. *Phys. Status Solidi A* **1986**, *97*, 243–247.
- (21) Grosse, P. *Free Electrons in Festkörpern*; Springer-Verlag: Berlin, 1979.
- (22) de Faria, D. L. A.; Silva, S. V.; de Oliveira, M. T. *J. Raman Spectrosc.* **1997**, *28*, 873–878.
- (23) Varadwaj, K. S. K.; Panigrahi, M. K.; Ghose, J. *J. Solid State Chem.* **2004**, *177*, 4286–4292.
- (24) Fu, Y. Y.; Wang, R. M.; Xu, J.; Chen, J.; Yan, Y.; Narlikar, A. V.; Zhang, H. *Chem. Phys. Lett.* **2003**, *379*, 373–379.
- (25) Davydova, N. A.; Tishchenko, V. V.; Baran, J.; Vlcek, M. *J. Mol. Struct.* **1998**, *450*, 117–120.
- (26) Mycroft, J. R.; Nesbitt, H. B.; Pratt, A. R. *Geochim. Cosmochim. Acta* **1995**, *59*, 721–733.
- (27) Moulder, J. F.; Stickle, W. F.; Sobol, P. E.; Bomben, K. D. In *Handbook of X-ray Photoelectron Spectroscopy*; Chastain, J., King, R. C., Jr.; Eds.; Physical Electronics, Inc.: Eden Prairie, MN, 1995.
- (28) Seah, M. P. In *Practical Surface Analysis*; Briggs, D., Seah, M. P., Eds.; John Wiley and Sons: New York, 1990; Vol. 1.
- (29) Buckley, A. N.; Woods, R. *Appl. Surf. Sci.* **1985**, *22/23*, 280–287.
- (30) Bonnisel-Gissinger, P.; Alnot, M.; Ehrhardt, J. J.; Behra, P. *Environ. Sci. Technol.* **1998**, *32*, 2839–2845.
- (31) Toniazzo, V.; Mustin, C.; Portal, J. M.; Humbert, B.; Benoit, R.; Erre, R. *Appl. Surf. Sci.* **1999**, *143*, 229–237.
- (32) Smart, R. S. C.; Skinner, W. M.; Gerson, A. R. *Surf. Interface Anal.* **1999**, *28*, 101–105.
- (33) Mycroft, J. R.; Bancroft, G. M.; McIntyre, N. S.; Lorimer, J. W.; Hill, I. R. *J. Electroanal. Chem.* **1990**, *292*, 139–152.
- (34) Eckert, B.; Steudel, R. *Top. Curr. Chem.* **2003**, *231*, 31–98.
- (35) Bubert, H.; Jente, H. *Surface and Thin Film Analysis: Principles, Instrumentation, and Applications*; Wiley-VCH: Weinheim, Germany, 2002.
- (36) Chen, J. G. *Surf. Sci. Rep.* **1997**, *30*, 1–152.
- (37) Wilken, R. T.; Barnes, H. L. *Geochim. Cosmochim. Acta* **1996**, *60*, 4167–4179.
- (38) Gagnon, C.; Mucci, A.; Pelletier, E. *Geochim. Cosmochim. Acta* **1995**, *59*, 2663–2675.
- (39) Mills, K. C. *Thermodynamic Data for Inorganic Sulphides, Selenides, and Tellurides*; Butterworths: London, 1974.
- (40) *CRC Handbook of Chemistry and Physics*; Lide, D. R., Ed.; CRC Press: Boca Raton, FL, 2005.
- (41) Verma, V. P. *Thermochim. Acta* **1999**, *327*, 63–67.
- (42) Campos, C. E. M.; de Lima, J. C.; Grandi, T. A.; Machado, K. D.; Drago, V.; Pizani, P. S. *Solid State Commun.* **2004**, *131*, 265–270.
- (43) Campos, C. E. M.; de Lima, J. C.; Grandi, T. A.; Machado, K. D.; Pizani, P. S. *Physica B* **2002**, *324*, 409–418.
- (44) Nagata, K.; Ishibashi, K.; Miyamoto, Y. *Jpn. J. Appl. Phys.* **1981**, *20*, 463–469.
- (45) Guo, F. Q.; Lu, K. *Phys. Rev. B* **1998**, *57*, 10414–10420.
- (46) Poborchii, V. V.; Kolobov, A. V.; Tanaka, K. *Appl. Phys. Lett.* **1998**, *72*, 1167–1169.
- (47) Bogomolov, V. N.; Poborchy, V. V.; Romanov, S. G.; Shagin, S. I. *J. Phys. C: Solid State Phys.* **1985**, *18*, L313–L317.
- (48) Lucovsky, G.; Mooradian, A.; Taylor, W.; Wright, G. B.; Keezer, R. C. *Solid State Commun.* **1967**, *5*, 113–117.
- (49) Kaplow, R.; Rowe, T. A.; Averbach, B. L. *Phys. Rev.* **1968**, *168*, 1068–1079.
- (50) Goldbach, A.; Johnson, J.; Meisel, D.; Curtiss, L. A.; Saboungi, M. L. *J. Am. Chem. Soc.* **1999**, *121*, 4461–4467.
- (51) Oremland, R. S.; Herbel, M. J.; Blum, J. S.; Langley, S.; Beveridge, T. J.; Ajayan, P. M.; Sutto, T.; Ellis, A. V.; Curran, S. *Appl. Environ. Microbiol.* **2004**, *70*, 52–60.
- (52) Bach, W.; Edwards, K. J. *Geochim. Cosmochim. Acta* **2003**, *67*, 3871–3887.